ARTICLE OPEN

Check for updates

On the role of Al/Nb in the SCC of AFA stainless steels in supercritical CO_2

Shuo Cong[1,4], Zhaodandan Ma[2,4], Zhu Liu[1], Zhengang Duan[2], Zhangjian Zhou[3], Lefu Zhang[1] and Xianglong Guo[1]✉

SCC of a series of AFA stainless steels with different Al and Nb contents were studied in supercritical CO_2 by SSRT. The results show that Nb element plays a precipitation strengthening on the mechanical properties, while it shows few effects on the corrosion properties. The surface oxide film of the Al-free material only consisted of amorphous Cr_2O_3 and Cr-rich spinel. With the addition of Al, the Al_2O_3 layers are formed and significantly decreases the element diffusion, thus inhibiting the initiation of SCC. Fe_3O_4 fills the interior of cracks of both Al-free and Al-containing materials. The Al_2O_3 layer is formed at the crack tip of Al-containing materials. Because the matrix grains are large, the protective Al_2O_3 layer can only be formed at the crack tip, which cannot completely hinder the outward diffusion of ions on the crack walls and its protective effect on the crack propagation is limited.

npj Materials Degradation (2022)6:56 ; https://doi.org/10.1038/s41529-022-00258-w

INTRODUCTION

With the advantages of high compact ability, good compressibility, and high heat transfer efficiency[1,2], supercritical carbon dioxide (sCO_2) has been considered as a potential fluid for different energy systems, such as nuclear reactors. The sCO_2 cooled nuclear reactor has become one of the most promising Generation IV nuclear reactors[3–7]. However, the failure of materials under the operating environment has gradually become one of the key issues that limit the development of the sCO_2 system[8].

Currently, the conventional structural and cladding materials that may be used in sCO_2 cooled nuclear reactor mainly include ferritic/martensitic (F/M) steel[9], austenitic stainless steel[10,11], and nickel-based alloy[12]. Among them, Ni-based alloys have high radioactive residue, but their economic cost is too high to be applied on a large-scale[13]. High-temperature corrosion resistance of F/M steels is poor[14]. The thickness of oxide film on T22 steel was beyond 32 μm after 200 h exposure in 550 °C sCO_2[9]. For the austenitic stainless steels and F/M steels exposed to low-temperature environment (such as subcritical water), Cr_2O_3 and Cr-containing oxide layers are formed on the surface, which plays the most important protective role[15]. But the stability of these Cr oxide films in high-temperature sCO_2 is still insufficient[10,16–18]. Large area spallation of oxide film and many porosities were observed on the surface of 310 and 316 stainless steels exposed to sCO_2 for only 500 h[10], which cannot meet the requirements for the applications in sCO_2-cooled nuclear reactor, especially the cladding materials.

To solve this problem, a material that not only owns high oxidation resistance in sCO_2, but also keeps the advantages of easy processing and low cost, is needed. Thus, the alumina-forming austenitic (AFA) stainless steels that initially developed to improve the creep resistance[19–24] have attracted more and more attention. Previous research showed that the mass gain of AFA steels in 800 °C air[25] and supercritical water[26] is quite low for the reason that a continuous Al_2O_3 layer was formed. Alumina (Al_2O_3) owns a lattice of corundum type, which is the same as Cr_2O_3, while the thermodynamic stability of Al_2O_3 is higher[22] and is expected to offer better protection to the materials[27–29] exposed to high temperature and corrosive environment. Pint et al.[30] compared the CO_2 pressure compatibility of several commercial Fe- and Ni-based structural alloys, and found that the mass gain of Al-containing materials was the lowest. The oxide film of AFA-OC6 in sCO_2 was mainly composed of thin and continuous Al_2O_3 and $(Cr, Mn)_3O_4$ at low temperatures or after short exposure time, while the oxide film showed a complex multilayer structure as the temperature and exposure time increased[31]. Moreover, with the addition of Al, the formation of Ni-Al phases[20–24,32,33] in the materials also increases the creep strength of materials, which future improves the application potential for AFA steels in high-temperature sCO_2 environment. The general corrosion resistance of steels was also enhanced in the lead-bismuth eutectic with the increasing of Al addition, while the continuous Al-rich oxide film formed only when the oxygen concentration was low[34,35].

However, the early research mainly focused on the general corrosion behavior of AFA steels, the mechanical property of AFA steels was mostly tested in air[19–24,36]. Few mechanical tests on AFA steels have been carried out in sCO_2. In practice, chemical corrosion and mechanical stress are acting on the materials simultaneously, which may result in the stress corrosion cracking (SCC) of the materials and plays one of the most significant roles in component failures of light water reactors (LWRs)[37]. It is reported that sCO_2 accelerated the cracking of materials at constant load[38]. Sridharan et al.[39] assessed the SCC of 316 and alloy 230 in sCO_2 using U-bend samples, and reported that the stress acting on the U-bend did not promote SCC nor significantly change the oxidation products. Olivares et al.[40] performed sCO_2 corrosion tests on high-Ni alloys pipes that were internally pressurized, and found that the internal oxidation rate was higher due to the internal pressure. The formation of oxide film on the surface is expected to affect the mechanical behavior of the materials[41,42]. Unfortunately, for AFA steels, the SCC behavior in sCO_2 has not been carefully studied, and the failure mechanism is not revealed.

For the effect of Nb, Shi et al.[43] studied the corrosion behavior of an AFA alloy with a composition of Fe-(15.2–16.6)Cr-(3.8–4.3)Al-

[1]School of Nuclear Science and Engineering, Shanghai Jiao Tong University, No. 800 Dongchuan Road, 200240 Shanghai, PR China. [2]Science and Technology on Reactor Fuel and Materials Laboratory Nuclear Power Institute of China, 610041 Chengdu, China. [3]School of Materials Science and Engineering, University of Science and Technology Beijing, 100083 Beijing, PR China. [4]These authors contributed equally: Shuo Cong, Zhaodandan Ma. ✉email: guoxianglong@sjtu.edu.cn

(22.9–28.5)Ni (wt.%) in 600 °C and 650 °C oxygen-containing molten Pb, and the results showed that a minor Nb addition increased the Cr availability, supported the earlier Cr_2O_3 formation, and triggered/enhanced the precipitation of B2-NiAl phase, which served as Al reservoir for the formation of Al_2O_3. In 1200 °C steam, it was reported that Nb addition increased the oxide adherence of $Al_{(7.9–8.9)}Cr_{(21.4–23.2)}Ni_{(34.3–35)}Fe_{bal}$(at.%) alloy, which reduced the oxide film exfoliation and increased the oxidation resistance of materials[44]. While Shen et al.[45] thought that Nb addition had a negative effect on the oxidation resistance of Fe-25Ni–10Cr–4.5Al steels at 1050 °C because Fe_2Nb phase suppressed the outward diffusion of Al. For mechanical performance, secondary nanosized NbC not only enhanced the creep resistance of the Fe–25Ni–18Cr–3Al (wt.%) and 15Cr–15Ni austenitic stainless steel, but also increased high-temperature strength even after long-term aging[46,47]. But for AFA steels exposed to sCO_2, the effects of Al and Nb content on the corrosion and SCC mechanisms are still unclear, and more efforts are needed.

In this work, the SCC behavior of AFA steels with different Al and Nb contents exposed to sCO_2 at 600 °C/10 MPa were studied by the slow strain rate tensile (SSRT) tests. The fracture surface, crack density and size, and oxide film composition were quantitatively measured. Based on these results, the effects of Al and Nb on the crack initiation and growth of AFA steels in high-temperature and high-pressure sCO_2 were compared. And the working mechanisms of Al and Nb on SCC were proposed.

RESULTS AND DISCUSSION

Effect of Al and Nb on the fracture and dynamic strain aging behaviors

Fig. 1 shows the stress–strain curves and the corresponding photographs of the failed tensile samples. Slight necking and dark corrosion products can be observed on all samples. The yield strength (YS), ultimate tensile strength (UTS) and elongation of the samples are listed in Table 1. It can be found that the YS and the UTS increases with the increase of Al and Nb content (A3 > A2 > A1 > A0). The elongation of the material increases first and then decreases with the increase of Al, while Nb addition decreases the elongation.

The effect of Nb on the strength can be attributed to the precipitation of NbC[36] in the matrix. As present in Fig. 2, bright NbC precipitates exist in the materials. Nb has a large atomic number, and thus the Nb compound (NbC) shows a bright color in backscattering electron (BSE) images[20,21,24]. Transmission electron microscopy (TEM) is used to further identify NbC precipitates. The bright-field (BF) image, the nanobeam diffraction pattern and EDS

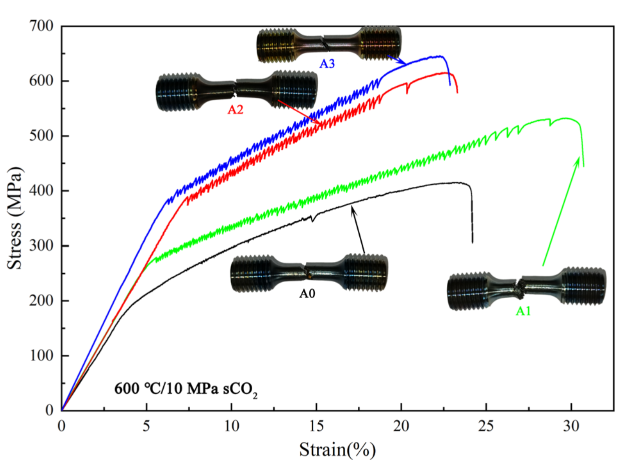

Fig. 1 SSRT stress–strain curves of different materials in sCO_2. (A0: 0Al-0.6Nb, A1: 2.5Al-0.6Nb, A2: 3.5Al-0.6Nb, A3: 3.5Al-1Nb).

dot scan results are shown in Fig. 2f, g, respectively. As shown in BSE images, most of NbC precipitates are distributed on grain boundaries (GBs) and a few of them are distributed inside the grains, which is consistent with former published results[20,21,24]. The size distribution of NbC is shown in Fig. 2e). NbC is a primary carbide, which precipitates directly from the liquid metal in the casting process. The SSRT process (aging happens simultaneously) has little effect on the content or the size of NbC. The volume fraction of NbC in different AFA samples is also measured. With the increase of Nb content from 0.6 wt. % to 1.0 wt.%, the volume fraction of NbC is also increased from 0.36 vol.%, 0.20 vol.%, 0.30 vol.% (A0–A2) to 0.72 vol.% (A3).

In the tensile process, NbC precipitates hinder the deformation of materials. In the meantime, NbC precipitates are mainly distributed at the grain boundaries, which contributes to stress concentration in this area and makes grain boundaries more prone to cracking. Thus, the materials with higher content of NbC precipitates are more propone to be cracked and exhibit a low elongation. Similar results were also reported by other researchers[48–50]. The internal cracks induced by NbC concentration are widely observed in the center of the samples, as shown in the following section. So, with the increase of Nb content, the toughness of material monotonically decreases. Because the solubility of Nb in the low carbon steel is very low (about 0.01%)[51,52], most of the Nb element is precipitated in the form of NbC. Therefore, the amount of solute Nb is negligible and its effect is not discussed in this study.

Al addition contributes to the formation of the NiAl phase in the steels, which increases the high-temperature strength of material[53]. However, in this study, there are not any Al-containing precipitates observed in the solid-solution treated samples before SSRT tests, as shown in Fig. 2a, which is consistent with the thermodynamic calculation results[33] in Fig. 2d. When the solid-solution temperature is higher than 860 °C, Al element is basically dissolved in the austenite lattice, and the amount of NiAl phase becomes zero. In this study, the material is water quenched after solid-solution treatment, so the Al element is kept being dissolved in the materials. However, Al-containing precipitates are formed in the SSRT tests. This is because the SSRT test is carried out at 600 °C, and the aging of the materials results in the precipitation of the Al-containing precipitates.

It has been reported that the addition of Al can increase the toughness of the material tested in corrosive environment through the formation of protective Al_2O_3 on the sample surface[8,25,54], which is consistent with the results of this study that the elongation of A1 is much higher than A0[8,25,54]. However, the elongation of the samples (A2 and A3) containing 3.5 wt.% Al is similar to A0 and lower than A1. As mentioned above, the increment of Al in AFA steels can influence the mechanical properties of the materials in two ways: on one hand, more Ni-Al precipitates are formed in 600 °C sCO_2 when the Al content is higher, so the strength of the materials is increased and the elongation is reduced; on the other hand, a high-level Al addition can increase the oxidation resistance of the materials, and hence to increase the toughness of the materials[8,25,54]. The combination of two mechanisms determines the final mechanical properties of the AFA steels, which will be further discussed in

Table 1. Chemical compositions of experimental materials (wt. %).

Element	Fe	Ni	Cr	Nb	Al	Mo	Si	C
A0 (0Al–0.6Nb)	Bal.	25	18	0.6	–	2	0.25	0.02
A1 (2.5Al–0.6Nb)	Bal.	25	18	0.6	2.5	2	0.25	0.02
A2 (3.5Al–0.6Nb)	Bal.	25	18	0.6	3.5	2	0.25	0.02
A3 (3.5Al–1Nb)	Bal.	25	18	1	3.5	2	0.25	0.02

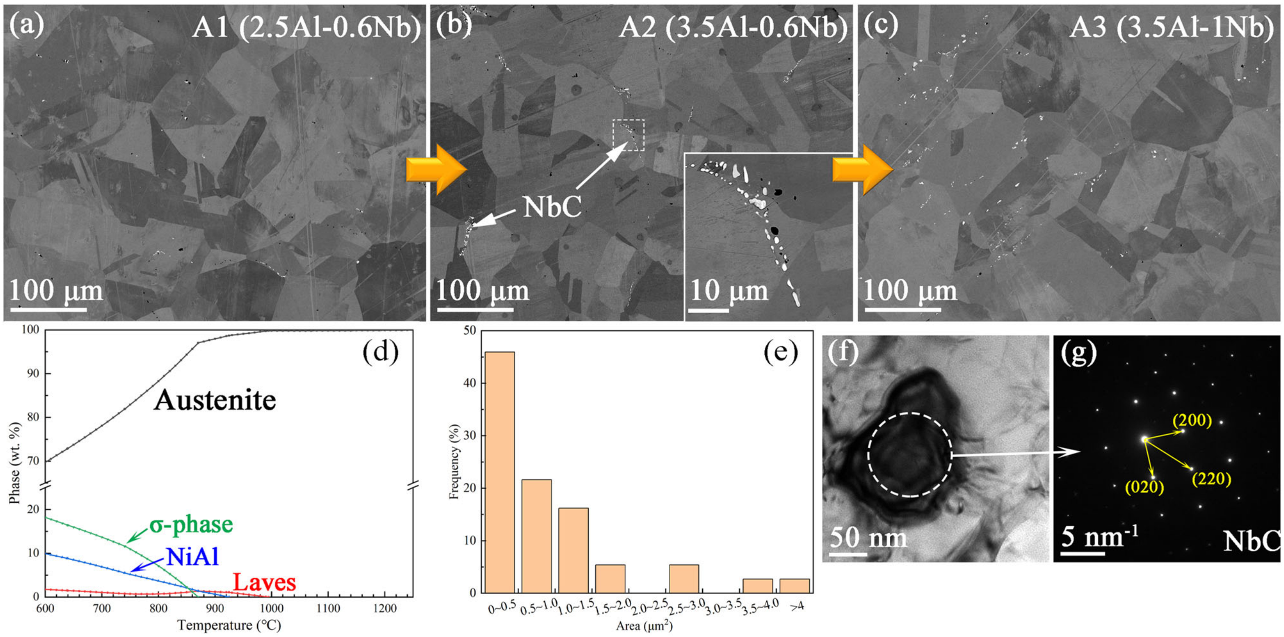

Fig. 2 Microstructure of AFA steels before tests. a–c BSE results of A1–A3 sample, **d** thermodynamic simulation of phase composition vs. temperature, **e** size distribution of NbC, TEM results of NbC precipitates (**f**) BF image and (**g**) nanobeam diffraction pattern of a NbC particle.

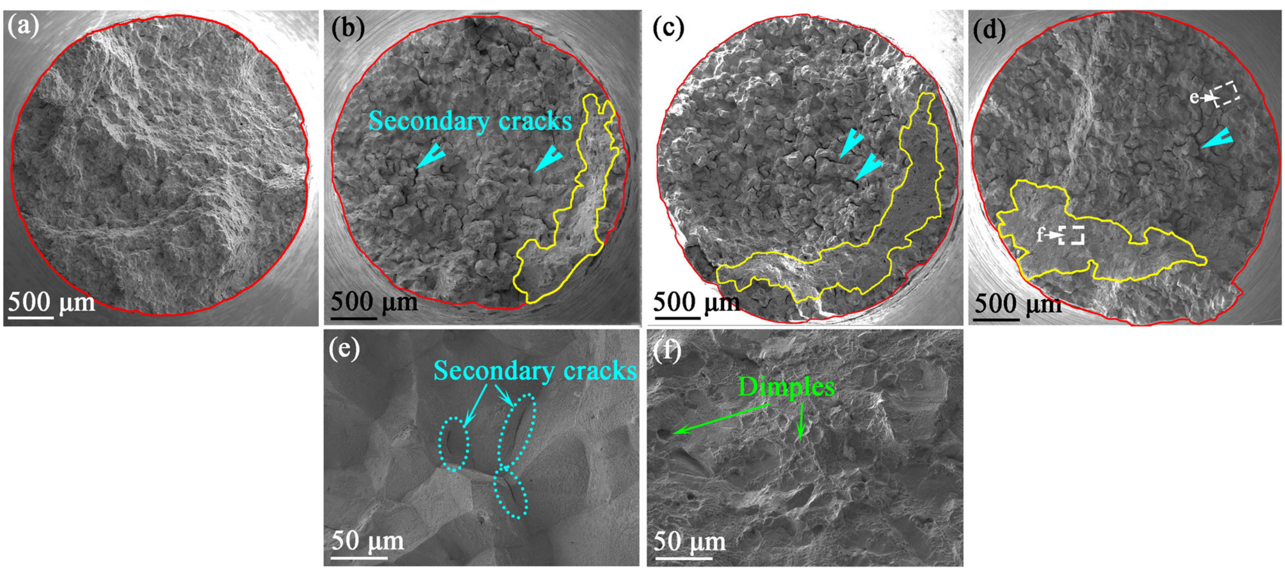

Fig. 3 Fractographies. a A0: 0Al-0.6Nb, **b** A1: 2.5Al-0.6Nb, **c** A2: 3.5Al-0.6Nb, **d** A3: 3.5Al-1Nb, **e** IGSCC pattern, and **f** ductile pattern in the white frame in (**d**).

the following paragraphs. In addition, the effects of Al and Nb on Young's modulus are also similar to their effects on strength, as shown in Fig. 1. With the increase of Nb or Al, the amount of NbC or Ni-Al precipitates increases, which inhibits the movement of dislocations and slip bands, leading to the increase of Young's modulus of materials. However, the displacement measuring device (the linear variable differential transformer, LVDT) cannot withstand the longtime exposure to high-temperature and high-pressure water, and it is installed outside the autoclave. The measured strain is inevitably higher than the true strain of the gauge section of the sample. So, the absolute value of Young's modulus is meaningless.

The tensile curve of the A0 sample (0Al–0.6Nb) is basically smooth. While under the same test conditions, the tensile curves of samples with Al addition (A1, A2, and A3) have obvious serrated yielding, which can be attributed to the dynamic strain aging (DSA) mechanism. This mechanism is summarized as follows: during the plastic deformation, the dislocations are pinned by some obstructions, leading to an increase in strength. Subsequently, the dislocations get rid of these obstructions and continue to move, which decreases the strength[55]. This process ultimately manifests as the serration flow and discontinuous plastic deformation. The DSA amplitudes of A1–A3 samples are 10.44 ± 2.62 MPa (2.5Al–0.6Nb), 14.05 ± 2.85 MPa (3.5Al–0.6Nb), and 12.04 ± 2.43 MPa (3.5Al–1Nb), respectively. The DSA value of the AFA steels with different Al contents is close, and more data is needed for a quantitative analysis of the effect of Al content on the DSA.

The fractographs of different samples are observed by scanning electron microscopy (SEM) and are shown in Fig. 3. The fracture of

Table 2. Data obtained from SSRT tests at 600 °C/10 MPa sCO_2.

No.	Composition	YS (MPa)	UTS (MPa)	Elongation at UTS (%)	DSA amplitude (MPa)	Section shrinkage (%)	IGSCC ratio (%)
A0	0Al–0.6Nb	182	415	23.5	0	13.8	100
A1	2.5Al–0.6Nb	277	532	29.7	10.44 ± 2.62	24.4	89.3
A2	3.5Al–0.6Nb	389	615	22.6	14.05 ± 2.85	14.3	84.7
A3	3.5Al–1Nb	385	646	22.3	12.04 ± 2.43	14.5	85.9

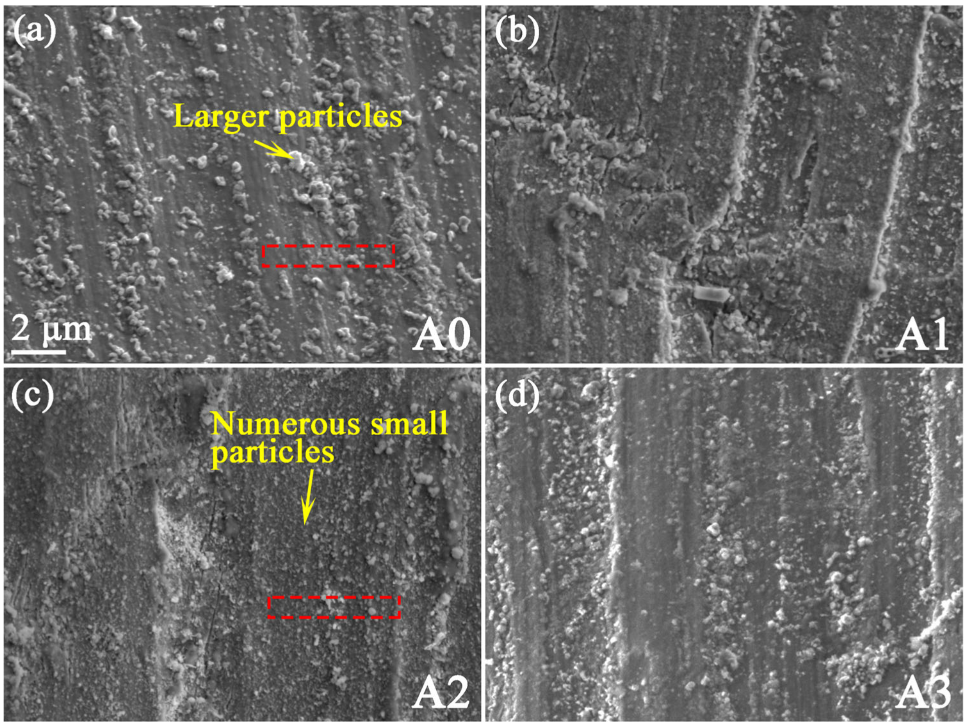

Fig. 4 Surface oxide films near the fractures. **a** A0 sample (0Al–0.6Nb), **b** A1 sample (2.5Al–0.6Nb), **c** A2 sample (3.5Al–0.6Nb), **d** A3 sample (3.5Al–1Nb).

each sample can be divided into two types of patterns: intergranular stress corrosion cracking (IGSCC) region and ductile fracture region. The IGSCC region is enlarged, as shown in Fig. 3e. The IGSCC pattern is observed in all samples and occupies most of the fracture, which indicates that the IGSCC tendency of all materials is high. Serval secondary intergranular cracks (marked by blue arrow) are also observed. Ductile fracture regions, whose typical pattern is shown in Fig. 3f, are composed of many dimples and occupy a small area on the fracture.

The fracture area and the ductile fracture regions of all samples are marked by red and yellow circles, respectively. And then the section shrinkage and the ratio of IGSCC are measured and listed in Table 2. The degree of necking is calculated by dividing the fracture area by the original section area. The IGSCC ratio is calculated by dividing the IGSCC area by the fracture area. As the data shows, 100% IGSCC occurs on the A0 sample. While with the addition of Al, the ductile fracture regions appear and occupy about 10–15% area of the fractures on A1, A2, and A3 samples. Among those samples, the A2 sample has the highest necking and a lower SCC tendency. Overall, for three kinds of materials containing Al element, the difference in IGSCC ratio is small. This indicates that the minor addition of Al (2.5 wt.%) has an obvious benefit effect on the SCC resistance, while the benefit effect is not further increased with the further increase of Al (from 2.5 wt.% to 3.5 wt.%).

Effect of Al and Nb on the oxide film composition and SCC initiation behavior

The surface oxide film has a dominant effect on the crack initiation during exposure to sCO_2. So, the oxide film is preferentially analyzed in this section. The morphologies of oxide films on the uncracked columnar surface of the tensile sample near the fracture are shown in Fig. 4. The oxides can be divided into two categories: the entire surface of the samples is covered with a continuous oxide film; and a few large oxide particles with an average dimension of ~0.3 µm are scattered on the oxide film. These large oxide particles are composed of 56.9 at.% O, 30.2 at.% Fe, 8.8 at.% Cr and 3.5 at.% Ni, according to SEM-EDS results. Referring to the results published, these particles are the spinel[10,56–60]. The distinguishable scratches on the surface of the samples after the SSRT tests indicate that the oxide film is quite thin. In the general corrosion process, the size of oxide particles on the surface of materials is an indication of the corrosion degree: the bigger the oxide particles, the higher the general corrosion degree. Among these samples, the oxide particles on the surface of A0 are the largest, indicating the most severe general corrosion degree of A0. With the addition of Al element, the size of oxide particles on the surface A1, A2, and A3 alloy decreases to about 0.2 µm, which indicates the corrosion resistance is improved. The improvement of corrosion resistance will benefit the SCC resistance of the materials.

The detailed cross-sectional microstructure of oxide film (uncracked part near the fracture, labeled by the red dash line box in Fig. 4 of A0 and A2 samples was studied by TEM, as shown in Figs. 5, 6, respectively. The maximum thickness of oxide film on the A0 sample is about ~560 nm, which contains an outer amorphous Cr_2O_3 layer and an inner Cr-rich spinel layer, as confirmed by the BF and high-angle annular dark field (HAADF) images of Fig. 5c, d. It has been reported that amorphous Cr_2O_3 is formed on the surface of Cr coated materials exposed to high-temperature CO_2[61,62]. Yue et al.[63] and Liu et al.[64] also reported that an amorphous layer mainly containing Cr_2O_3 was observed on the surface of API-P110 grade 13Cr and 2205 duplex stainless steel exposed to subcritical CO_2, while nano-polycrystalline oxide was formed in much higher temperature environment. In summary, the amorphous Cr_2O_3 is always present on the mildly corroded samples. Thus, it can be deduced that the formation of amorphous Cr_2O_3 is related to the relatively low corrosion degree of materials. In this study, the Cr content is relatively high, and the grain size of the sublayer is very small after grinding treatment, so the outward diffusion rate of Cr element is fast and a continuous Cr_2O_3 oxide layer is formed at the first time. The early formation of Cr_2O_3 leads to a low corrosion degree, and the Cr_2O_3 has not been sufficiently crystallized. As a result, the Cr_2O_3 exhibits an amorphous structure. The inner oxide layer is polycrystalline spinel. The EDS mapping in Fig. 5e shows that the main composition of this layer is Cr and O, and only a few Fe element is observed. So, this layer is composed of Cr-rich spinel.

According to the above results, the corrosion process can be summarized as follows: the amorphous Cr_2O_3 layer is formed first, and then some Fe ions penetrate into the amorphous Cr_2O_3 layer and react with Cr_2O_3, which results in the formation of the Fe–Cr spinel layer. While the outward diffused Fe ions are insufficient, and the Cr_2O_3 layer cannot be completely consumed. Thus, some residual Cr_2O_3 is still present at the top of the oxide film, and the spinel is present at the bottom of the oxide film. Pores are also observed at the oxide/matrix (O/M) interface, and the material surrounding those pores is also oxidized, as shown in Fig. 5b. The internal oxidation zone (IOZ) is observed along the grain boundaries. In the corrosion process, metal elements, such as Cr, Fe, and Al, diffuse outward to the surface to form the oxide film. In the meantime, the matrix becomes loose and the pores are formed. If these pores further grow up and connect with each other, they can develop into cracks.

As shown in Fig. 6, a multilayer oxide film with an average thickness of ~100 nm covers the surface of the A2 sample, which is much thinner and more compact than the oxide film on the A0 sample (~560 nm). As the oxide film becomes more compact, it is more difficult to be cracked in the tensile process. Specifically, the oxide film can be divided into three layers. Beneath two Cr-rich layers (amorphous Cr_2O_3 and polycrystalline Cr-rich spinel), the bottom layer is an Al_2O_3 polycrystalline layer. As shown in Fig. 6f, the Al_2O_3 layer is continuous and intact. Although the surface material is twisted in the SSRT test, the Al_2O_3 layer still almost covers the whole surface. Even for the microcrack in Fig. 6c, the Al_2O_3 also fills the crack interior, which inhibits the further corrosion and growth of the crack. With the formation of continuous Al_2O_3 layer, the outward diffusion of Fe ions is decreased, and the Fe element, which existed on the surface before the test, reacts with Cr_2O_3 and forms the spinel. Compared with the A0 sample, the thickness of Cr-rich spinel layer decreases as well, and no continuous Cr-rich spinel layer is formed. As shown in Fig. 6b, at places where the residual Fe content is higher, the spinel grows and forms a bulge. For Nb element, there are not any Nb-containing oxides observed in all SEM and TEM results. NbC precipitate is difficult to be oxidized and has little effect on the microstructure and composition of the oxide film. There are no obvious pores and the IOZ[65–68] in the Al-containing materials, which is because the inward diffusion of O is also inhibited by the Al_2O_3 layer. The comparison between the uncracked oxide film formed on the surface of A0 and A2 indicates that Al plays an important role in determining the corrosion behavior of the materials.

Beneath the oxide film, a NiAl denuded matrix alloy layer with average thickness of ~150 nm is formed. While a layer (average thickness of ~850 nm) with a high density of NiAl precipitates exists below the NiAl denuded layer. Both layers are located in the surface work-hardened area. In this area, the grain size is much smaller and the grain boundary density is higher, so precipitates (~100 nm) are formed in a short time (<100 h), as shown in Fig. 6d. In addition, the size of these precipitates in the surface work-hardened area decreases with the increase of depth. The volume fraction of the precipitates in the surface work-hardened layer (fine grains) is about 6.62%, while the value becomes less than 0.5% in the matrix alloy with coarse grains. According to the published results[19–24], precipitates would be formed during the aging treatment of AFA steels. The generating rate of precipitates is affected significantly by the element diffusion rate. In the fine grain region, the element diffusion rate is higher and the precipitates can grow larger. The disappearance of precipitates in the NiAl denuded layer is because Al element diffuses outward to the sample surface and form the surface Al-containing oxide film. The Cr-rich precipitate denuded layer is also observed in the work-hardened area, whose thickness is about 330 nm and it is thicker than NiAl denuded layer. This is because Cr ions have been diffused outward in this layer and the Cr-rich precipitate cannot be formed.

The oxide film of AFA steels tested in this study is different from those of other stainless steels corroded in a similar environment[10,56–60], which are usually composed of Fe_3O_4/Fe_2O_3[69], Fe-Cr-Ni spinel[70,71], Cr-rich layer and metallic Ni layer below the oxide film[72] from outside to inside. As shown in Fig. 7a, because the surface of the tensile sample before SSRT tests is rough (ground without polishing treatment), there is a surface work-hardened layer on the surface of the materials. In this layer, the grain size decreases obviously to 100–200 nm, and the density of GBs increases. In the meantime, large kernel average misorientation (KAM) values, which means large plastic deformation, also appear in the surface work-hardened layer, as shown in Fig. 7b. The increment of GB density provides more fast diffusion paths and accelerates the formation of Al_2O_3 or Cr_2O_3 layers[73], which inhibit the outward diffusion of Fe ions in the test (<100 h), so Fe_3O_4/Fe_2O_3 has not yet been formed. Furthermore, there is no obvious Ni-rich metallic layer[74] beneath the oxide film of the samples. The formation of the metallic Ni-rich layer is because the Fe and Cr ions diffuse outward, and the relative content of Ni increases[74]. In this study, the relative content of Ni changes little and the metallic Ni layer is not formed without the fast outward diffusion of Fe and Cr ions.

According to the above results, the formation process of oxide film in AFA steels exposed to sCO_2 is summarized and schematically shown in Fig. 8:

Because the content of Cr in the materials is much higher than Al, and Cr has a relative higher affinity with CO_2 than other elements except Al, dynamically, Cr reacts with CO_2 to form the continuous Cr_2O_3 layer (Fig. 8b) first on the sample surface:

$$2Cr + \frac{3}{2}CO_2(g) = Cr_2O_3 + \frac{3}{2}C,\ \Delta \boldsymbol{G} = -309.786\,\mathrm{kJ \cdot mol^{-1}} \tag{1}$$

Once the continuous Cr_2O_3 layer is formed, the oxygen partial pressure at the O/M interface becomes lower. Then only the Al element can be preferentially oxidized because of its highest affinity with oxygen. As shown in Fig. 8a, Al existed in the grains or precipitates can diffuse outward along the grain boundaries, and a continuous Al oxide layer is formed according to the

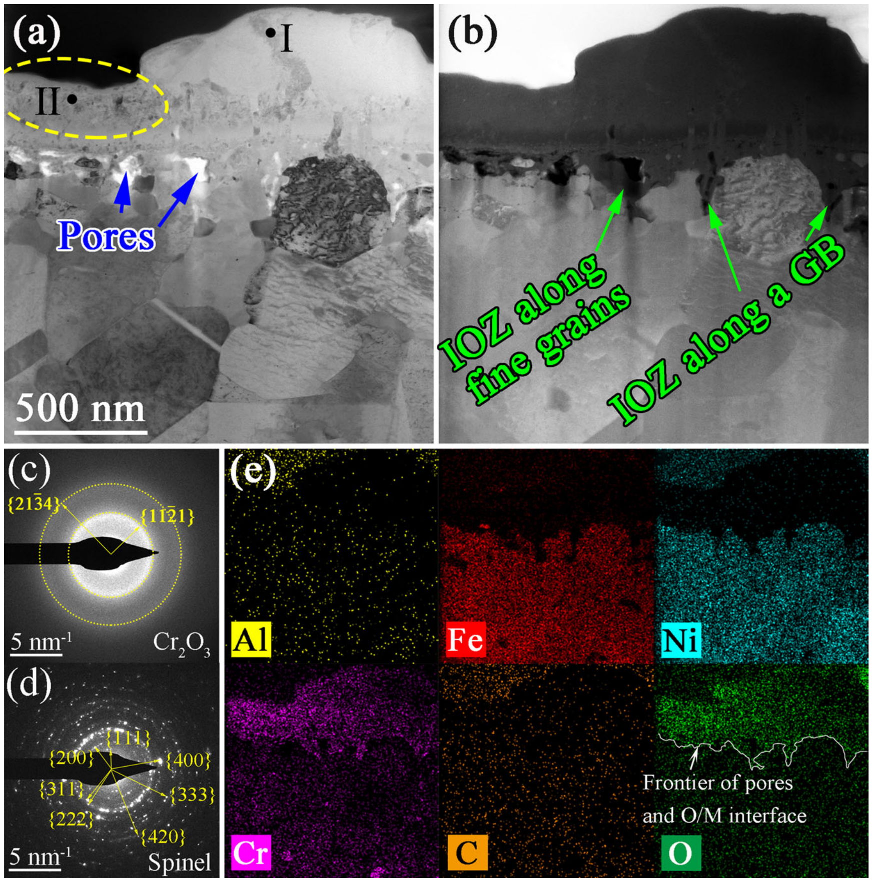

Fig. 5 TEM results of the surface oxide film of A0 sample. **a** BF image, **b** HAADF image, **c**, **d** Nanobeam diffraction patterns of I and II regions, **e** EDS mapping of (**a**).

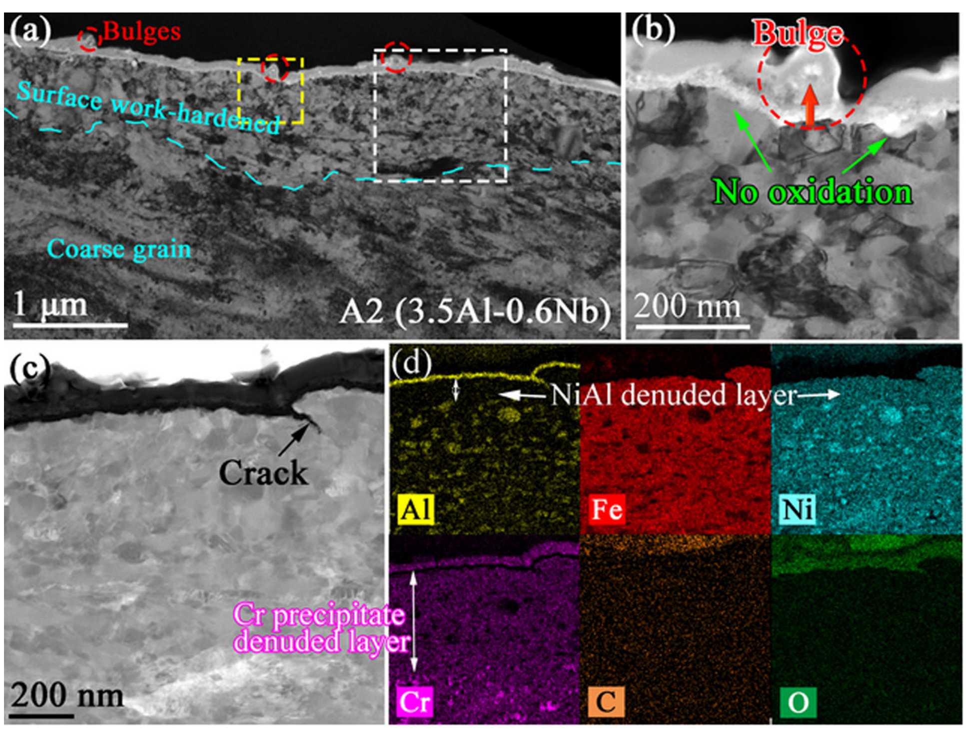

Fig. 6 TEM results of the surface oxide film near the fracture of A2 sample. **a** BF image, **b** magnification of the oxide film inside the yellow frame in (**a**), **c** HAADF image inside the white frame in (**a**), **d** EDS mapping of (**c**).

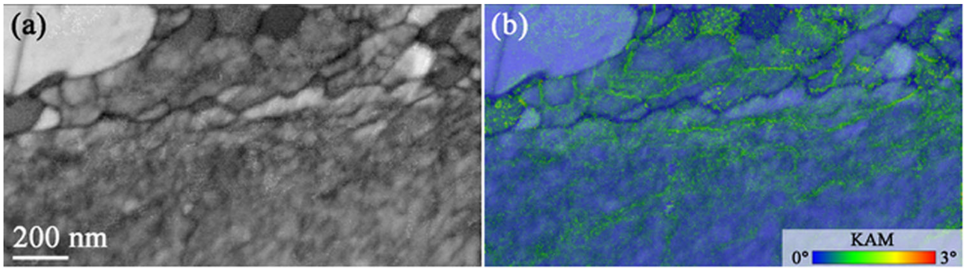

Fig. 7 TKD results of the surface work-hardened layer of A2 sample before SSRT tests. **a** Grain structure, **b** KAM mapping.

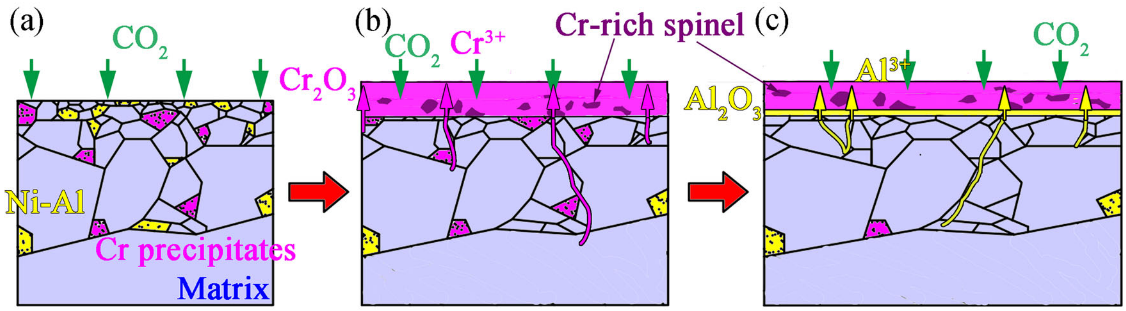

Fig. 8 Schematic corrosion process of AFA steel exposed to sCO_2. (**a**) the original state of the materials, (**b**) the formation of Cr_2O_3 layer, (**c**) the formation of Al_2O_3 layer.

following reaction:

$$2Al + \frac{3}{2}CO_2(g) = Al_2O_3 + \frac{3}{2}C,\ \Delta \boldsymbol{G} = -808.387\,\mathrm{kJ \cdot mol^{-1}} \quad (2)$$

Cr_2O_3 can restrain the outward diffusion of Ni but not Fe because Fe has a high solubility in Cr_2O_3[70]. In the Al-free stainless steels, the outward diffused Fe will react with Cr_2O_3 to form $FeCr_2O_4$ spinel at 600°C based on the following equations:

$$Cr_2O_3 + Fe + \frac{1}{2}CO_2(g) = FeCr_2O_4 + \frac{1}{2}C,\ \Delta \boldsymbol{G} = -9.483\,\mathrm{kJ \cdot mol^{-1}} \quad (3)$$

However, due to the formation of continuous Al_2O_3 layer, the outward diffusion of Fe is reduced in Al-containing materials. So, only a few residual Fe element, which already existed on the surface before the test, can react with Cr_2O_3. Cr-rich spinel is then formed.

Ni is hardly to be oxidized by CO_2 and combine with Cr_2O_3 to form $NiCr_2O_4$, according to the calculated Gibbs free energy at 600 °C as follows:

$$2Ni + CO_2(g) = 2NiO + C,\ \Delta \boldsymbol{G} = 76.379\,\mathrm{kJ \cdot mol^{-1}} \quad (4)$$

For Nb element, it has a little effect on the oxidation process. This is because Nb element mostly combines with C to form NbC in the cast process. The reaction between NbC and CO_2 is more difficult, as clearly indicated by the fact that the Gibbs energy of reaction (7) is less negative:

$$2NbC + CO_2(g) = 2NbO + 3C,\ \Delta \boldsymbol{G} = -14.694\,\mathrm{kJ \cdot mol^{-1}} \quad (5)$$

In summary, with the existence of Al_2O_3 at the O/M interface, the oxide film of the AFA steels is more intact and thinner. The outward diffusion of matrix element, the formation of IOZ and the pores at the O/M interface are inhibited by the continuous Al_2O_3 layer. Thus, the oxide film is hard to be cracked and reduce the probability of crack initiation. In contrast, without the Al addition, the oxide film is thicker. Pores and IOZ are formed at the O/M interface, which may easily develop into cracks in the tensile process.

Effect of Al and Nb on the propagation of SCC

To clearly reveal the effects of Al and Nb on the crack propagation of AFA steels, the microstructure and the composition of the formation of the area of the cracks are studied. As presented in Fig. 9a, the distribution of microcracks on the columnar surface is not uniform. Taking A2 as an example, the microcracks near the IGSCC fracture is sparse (surface A), while they are dense near the ductile fracture (surface B). This can be attributed to the reason that the formation of the main crack (which develops to fracture finally) releases part of the stress on the nearby surface A and consequently inhibit the initiation and growth of new cracks. In contrast, there is no main crack/stress release on surface B, so the high stress leads to the easier initiation and growth of new cracks.

The morphologies of the cracks near the ductile fractures (surface B) of different samples are also studied. As shown in the first row of Fig. 9c–f, the microcracks of the A1 sample are the widest and the longest. This is because the A1 sample shows the highest elongation in the SSRT test, and the microcracks can be fully developed in the longer testing time. The samples are split along the black lines in Fig. 9a, and the cross-sections of microcracks are observed and shown in the second row of Fig. 9c–f. It can be found that the cracks strictly grow along grain boundaries, which indicates that the IGSCC susceptibilities of all samples are extremely high.

In addition, few NbC precipitates are observed on the crack growth paths or in front of the crack tips, which indicates that NbC precipitates have little effect on the growth of SCC cracks in this work. This is because NbC is not uniformly distributed on the grain boundary and concentrated at certain areas. Thus, the cracks initiated from the seriously corroded regions are difficult to encounter and be affected by NbC. According to the results of Qiao et al.[75], Nb hardly affected the SCC susceptibility of low-alloy steels in seawater without hydrogen charging. While Shi et al.[43] reported that Nb addition could increase the Cr availability in the matrix by reducing the formation of carbide, which supported the earlier Cr_2O_3 formation and thus improved the SCC resistance of material. In our work, the NbC precipitates are large and concentrated at part of grain boundaries, which results in stress concentration and the development of the creep cracks

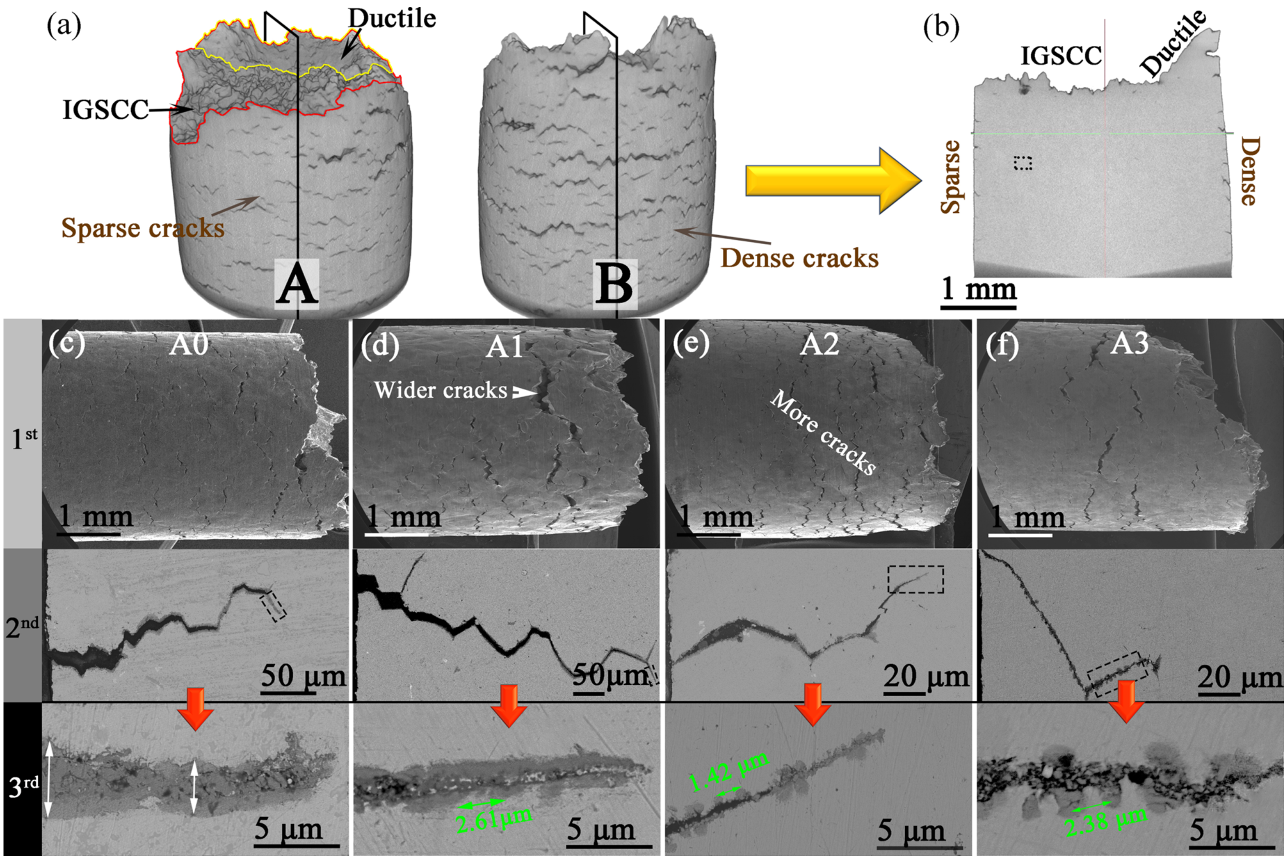

Fig. 9 Feature of surface microcracks. a Surface microcracks of A2 sample observed from different angles, **b** schematic diagram of cross-section processing, surface microcracks observed from the top and the cross-section of (**c**) A0 sample (0Al–0.6Nb), **d** A1 sample (2.5Al–0.6Nb), **e** A2 samples (3.5Al–0.6Nb), **f** A3 samples (3.5Al–1Nb).

developed inside the materials. As shown in Fig. 10a, many bright NbC precipitates are located at both ends of the creep crack, which is existed inside the material and uncorroded. Several micropores are formed near these NbC precipitates. This indicates that the aggregated NbC precipitates promote the initiation and the growth of internal creep cracks. So, with the increase of Nb content, the toughness of the sample decreases.

A comparison between the surface cracks shown in the third row of Fig. 9c–f and the internal cracks shown in Fig. 10b indicates that there are obvious oxidation regions on the surface crack walls. The oxide film on the crack wall of the A0 sample is the thickest, which reaches 4.5 μm in many places. While the thickness of the oxide films on the crack walls of A1–A3 samples is ranged from 0 μm to 2 μm, suggesting a higher corrosion resistance of the materials. It should be also noticed that the thickness of the crack walls oxide films of A1–A3 samples is not uniform. The oxide films become thicker at intervals, indicating that the oxidation process of the materials is discontinuous. It is generally believed that the stress corrosion cracking is occurring via a slip-film rupture-oxidation mechanism[76,77]. The growth of cracks is accompanied by the formation and the rupture of oxide film again and again. In this iterative process, the crack intermittently grows and arrests, resulting in intermittent changes in the thickness of the oxide films on the crack walls. The related mechanism is discussed in detail in the following paragraphs.

To better analyze the crack growth process, the microstructure and the composition of the crack tips of A0 and A2 samples are studied, as shown in Figs. 11–13, respectively. Figure 11 shows the oxide film on the crack walls of the A0 sample. In Fig. 6, the corrosion in the crack initiation process occurs on the surface work-hardened layer with fine grains. While the corrosion in the crack growth process (Figs. 11–13) occurs on the large matrix grains. Therefore, the structure of oxide film is different.

With the large grains, the outward diffusion rate of Al and Cr is decreased, and the formation of continuous Al_2O_3 and Cr_2O_3 layers is hindered. Except the Cr-containing spinel, Fe_3O_4 is also formed and fills the crack crevice, regardless of the sample type, as shown in the selected area electron diffraction (SAED) pattern results in Figs. 11–13. Furthermore, metallic Ni layer is also observed near the grain boundary, as shown in the EDS mapping results of Fig. 11, which is because Fe diffuses outward, and the relative content of Ni in this layer is increased. As shown in Fig. 11b, the material on both sides of the cracked grain boundary is corroded seriously and deeply. This is because the element diffusion along the grain boundary is faster than through the intercrystallite, which contributes to the earlier formation of protective oxide film above the grain boundary and inhibits serious corrosion. Similar to the uncracked surface, a selective oxidation zone is also observed.

Figure 12a clearly shows that the crack walls of A2 samples are also oxidized in the cracking process, and the crack is filled with oxides. The width of the crack in the A2 sample is uneven because the crack intermittently grows and arrests. In the crack-arrest period, the crack wall near the crack tip is more seriously oxidized, as shown in Fig. 12a. The composition of the materials near the crack tip is analyzed by EDS and the results are shown in Fig. 12c–g. It can be concluded that the oxides formed during the crack-arrest period include four kinds of species: Fe_3O_4 filling in the crack center (region II), Cr_2O_3 (region III), Cr-rich spinel (region IV), and an extremely thin Al_2O_3 layer surrounding the crack tip. As shown in Fig. 12c, the shorter the distance to the crack tip, the thicker the Cr-containing oxide layer or the Al_2O_3 layer. Although the Al_2O_3 layer is formed at the crack tip, the coverage of the Al_2O_3 layer at the crack tip is not

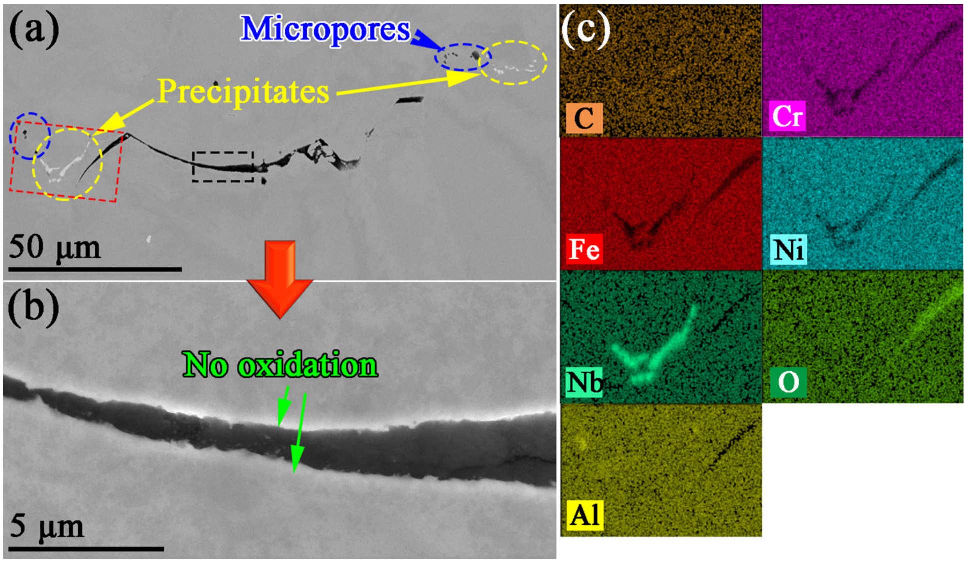

Fig. 10 Internal microcracks in the dark frame of Fig. 9b (A2 sample, 3.5Al–0.6Nb). **a**, **b** BSE images, **c** EDS in the red frame of (**a**).

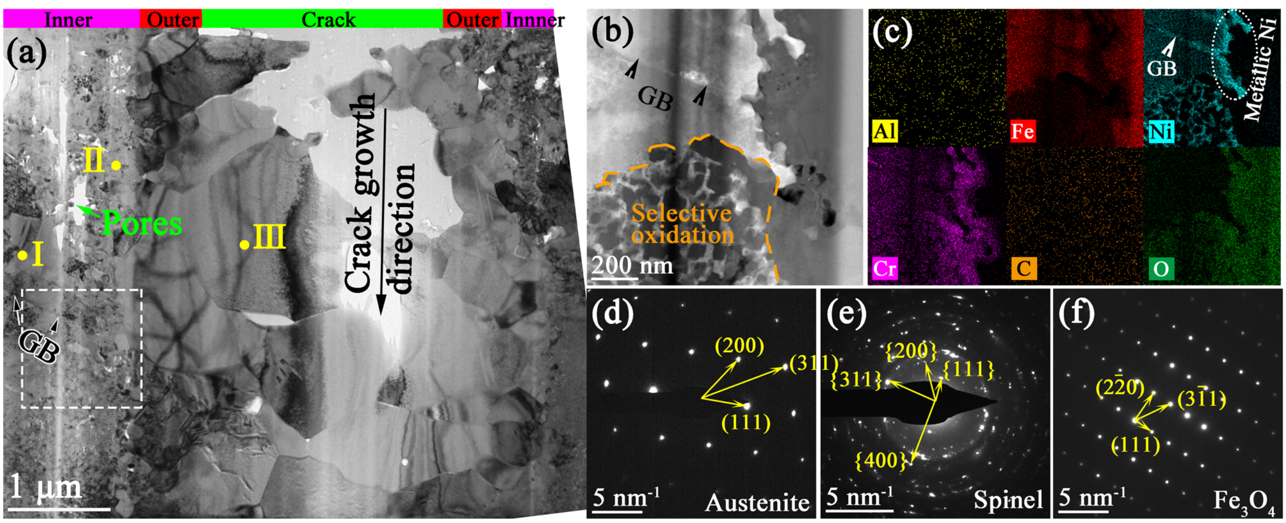

Fig. 11 TEM results near the crack tip of A0 sample (0Al–0.6Nb). **a** BF image, **b** HAADF image inside the white frame, **c** EDS mapping of (**b**), **d**–**f** SAED patterns of I, II and III regions labeled in (**a**).

large enough to completely inhibit the outward diffusion of Fe in the area relatively far from the crack tip.

Different from the grains in the surface work-hardened layer, the matrix grain size is large, and the grain boundary density is low. In this condition, the formation of a continuous Al_2O_3 layer is difficult. As shown in the EDS mapping results of Figs. 12, 13, the Al_2O_3 layer is not obvious. But stress and strain fields exist at the crack tip, as pointed out by Andresen[78,79], which greatly accelerates the element diffusion in this area and contributes to the formation of relatively thick Cr_2O_3 and Al_2O_3 layer. The formation rate of the Cr_2O_3 and Al_2O_3 layers decreases rapidly as the distance to the stress concentration area increases, and the Cr_2O_3 and Al_2O_3 layers are only formed in a very small area near the crack tip.

Figure 13 shows the oxide film formed on the crack walls of the rapid crack propagation stage labeled by the green frame in Fig. 12. The width of the crack is about 150 nm. As shown in Fig. 13a, the crack is filled with oxides, and the center consists of Fe_3O_4. However, compared to the oxide film at the crack tip in Fig. 12b, the Cr_2O_3 layer is fragmented, and no Al_2O_3 layer is observed.

Based on the above results, the process of the crack growth of AFA steels and the effect of Al addition can be summarized and schematically described in Fig. 14 as follows:

Firstly, because of the stress concentration at the crack tip, many lattice defects are produced and the element diffusion is accelerated (stage I). So, at the crack tip (the plastic deformation in this area is the largest), the Al_2O_3 layer is formed for the fast outward diffusion rate. The concentration of Cr in the matrix is high, so Cr_2O_3 oxide film is also formed on the crack walls exposed to sCO_2. In the meantime, Fe ions diffuse outward through the discontinuous Al_2O_3 and Cr_2O_3 layer to form Fe_3O_4, which fill the narrow crevice, as shown in Fig. 14b. Fe ions can also react with Cr_2O_3 to form Cr-rich spinel. At stage III, the crack tip oxide film is ruptured by the applied load, the crack advances one step along the grain boundary and the fresh metal is exposed to sCO_2 again, as shown in Fig. 14c. Because the duration of cracking of the crack tip oxide film is short, the crack growth path is corroded mildly. The length of a step can usually reach several microns, as shown in Fig. 9, which is similar to the formation of crack-arrest markings[80–83]. As the crack grows, the material near

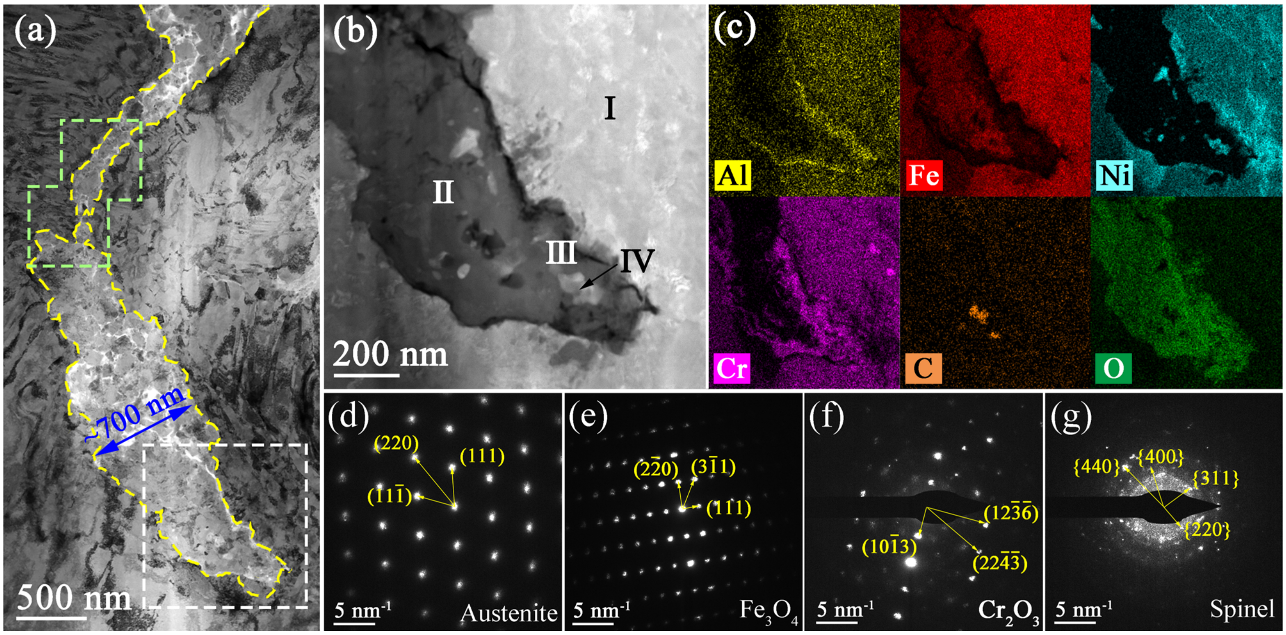

Fig. 12 TEM results of the crack tip of A2 sample (3.5Al–0.6Nb). **a** BF image, **b** HAADF image inside the white frame, **c** EDS mapping of (**b**), **d**–**g** nanobeam diffraction patterns of I, II, III and IV regions labeled in (**b**).

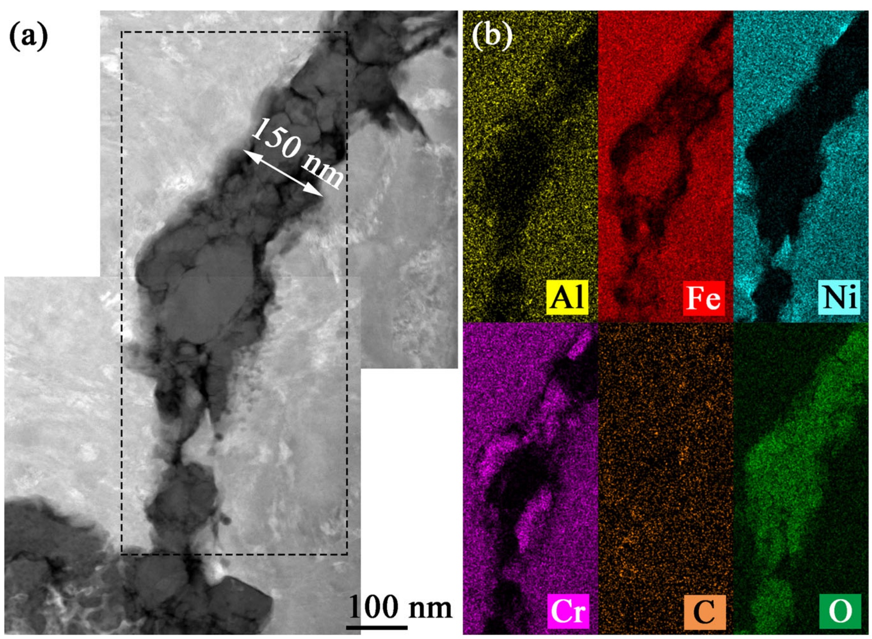

Fig. 13 TEM results of the crack path inside the green frame in Fig. 12a. **a** HAADF image, **b** EDS mapping of (**a**).

the new crack tip is corroded quickly and Al_2O_3/Cr_2O_3 layer can be formed again. Subsequently, the same corrosion process as stage II occurs repeatedly, as schematically shown in Fig. 14d. Finally, a thick-thin discontinuous oxide film is formed in the slip-film rupture-oxidation process, and the crack grow inward intermittently along the grain boundary.

METHODS

Materials

AFA steels used in this study were provided by University of Science and Technology Beijing (USTB). The chemical composition of AFA steels is shown in Table 2. The materials were firstly fabricated by vacuum induction melting. Then the casts were forged in the temperature range from 1250 °C to 1050 °C with a 3:1 forging ratio, and homogenized at 1150 °C for 2 h. At last, hot rolling was performed on the homogenized materials for three times with a reduction ratio of 20% each time, and then the rolled materials were solution treated at 1200 °C for 2 h. The materials were machined to tensile samples with a gauge section of Φ 3.6 × 8 mm, as presented in Fig. 15a. The surfaces of the tensile samples were abraded with 180# emery papers, ultrasonically rinsed with alcohol, and dried before the SSRT tests.

SSRT tests

SSRT tests were carried out in sCO_2 at 600 °C and 10 MPa. The testing system is schematically shown in Fig. 15b. CO_2 with the purity of 99.99% was used. The system includes two thermocouples that are located above

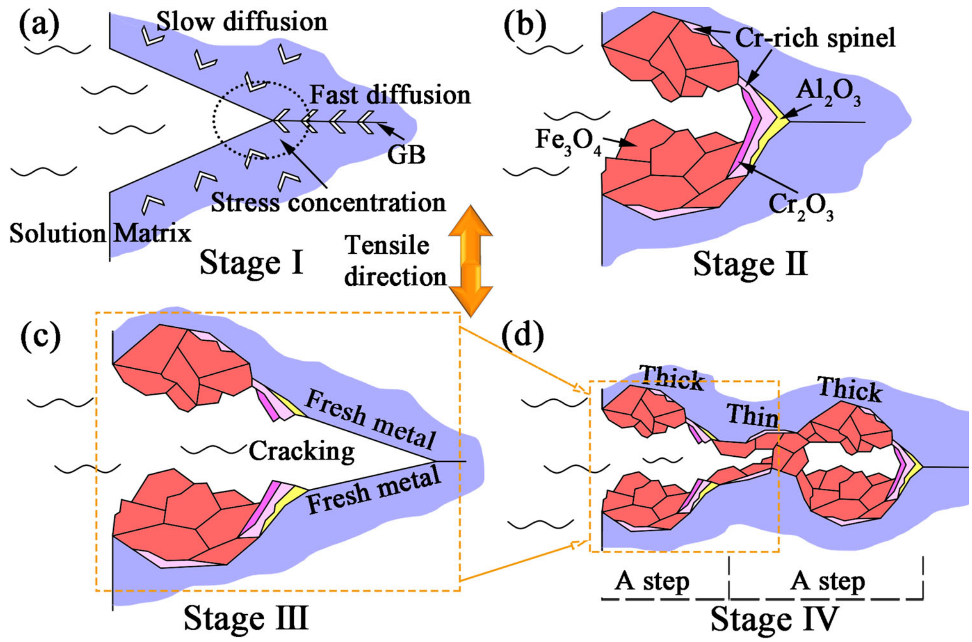

Fig. 14 Schematic crack growth process of AFA steel exposed to sCO_2. (**a**) the original state and the diffusion of elements at different positions at the crack tip, (**b**) the formation of the oxide scale at the crack tip, (**c**) the fracture of the oxide scale and the growth of the crack, (**d**) the formation of oxide scale on the fresh surface.

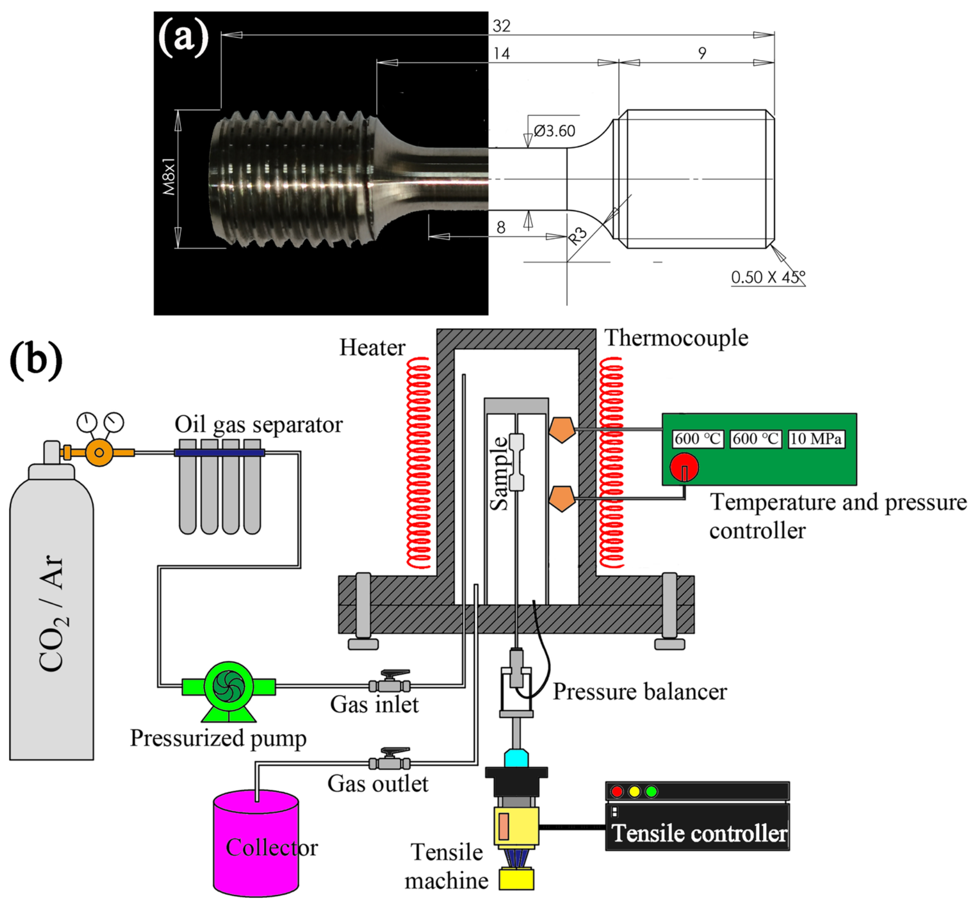

Fig. 15 Schematic diagram. a The tensile sample, **b** the SSRT autoclave system.

and below the tensile sample to ensure the accuracy of testing temperature. The system also includes a pressure balancer to balance the pressure between the autoclave and the tensile sleeves, so as to ensure the accuracy of force. Before tests, the autoclave was flushed with CO_2 for three times to remove the residual air in the system. The tensile rate was selected according to the crosshead speed and the gauge lengths of the samples, and a strain rate of $1 \times 10^{-6}\,s^{-1}$ was applied.

Microstructure characterization methods

The microstructure of the samples before and after SSRT tests was characterized by SEM BSE mode on a Tescan Mira3. The fracture surfaces and the oxide film on the sample surfaces were observed using SEM secondary electron mode on a Tescan Rise Magna. The detailed microstructure and the composition of oxide film/crack tip were studied by TEM on a Talos F200X. The cross-sectional TEM samples were cut using the focused ion beam (FIB) technique on a Hitachi NB5000. The elemental distributions were measured by Energy Dispersive Spectroscopy (EDS). The structure and the residual stain of the surface work hardening layer of samples before SSRT tests were analyzed by transmission kikuchi diffraction (TKD) on a Mira3.

DATA AVAILABILITY

The raw/processed data required to reproduce these findings can be shared if some researchers are interested in this study. At this time, the raw/processed data will not be submitted, as the data form part of ongoing projects.

CODE AVAILABILITY

No code is used in this study and needs to be summited.

Received: 27 December 2021; Accepted: 26 May 2022;
Published online: 12 July 2022

REFERENCES

1. Stepanek, J. et al. Parametric study of S-CO_2 cycles for the DEMO fusion reactor. *Fusion Eng. Des.* **160**, 111992 (2020).
2. Wu, P. et al. Preliminary safety evaluation of a supercritical carbon dioxide Brayton cycle cooled reactor system under loss-of-flow accident. *Nucl. Eng. Des.* **369**, 110860 (2020).
3. Dostal, V., Driscoll, M. J. & Hejzlar, P. A Supercritical Carbon Dioxide Cycle for Next Generation Nuclear Reactors. Thesis, Massachusetts Institute of Technology, Department of Nuclear Engineering, 1 (2004).
4. Khatoon, S., Ishaque, S. & Kim, M.-H. Modeling and analysis of air-cooled heat exchanger integrated with supercritical carbon dioxide recompression Brayton cycle. *Energy Convers. Manag.* **232**, 113895 (2021).
5. Gao, C. et al. Preliminary study of system design and safety analysis methodology for supercritical carbon dioxide Brayton cycle direct-cooled reactor system. *Ann. Nucl. Energy.* **147**, 107734 (2020).
6. Crespi, F. et al. Supercritical carbon dioxide cycles for power generation: a review. *Appl. Energy.* **195**, 152–183 (2017).
7. Firouzdor, V. et al. Corrosion of a stainless steel and nickel-based alloys in high temperature supercritical carbon dioxide environment. *Corros. Sci.* **69**, 281–291 (2013).
8. Li, K., Zeng, Y. & Luo, J.-L. Corrosion of SS310 and Alloy 740 in high temperature supercritical CO2 with impurities H_2O and O_2. *Corros. Sci.* **184**, 109350 (2021).
9. Zhu, Z. et al. Corrosion behavior of ferritic and ferritic-martensitic steels in supercritical carbon dioxide. *Energy* **175**, 1075–1084 (2019).
10. Cao, G. et al. Corrosion of austenitic alloys in high temperature supercritical carbon dioxide. *Corros. Sci.* **60**, 246–255 (2012).
11. Holcomb, G. R., Carney, C. & Doğan, Ö. N. Oxidation of alloys for energy applications in supercritical CO_2 and H_2O. *Corros. Sci.* **109**, 22–35 (2016).
12. Pint, B. A. & Keiser, J. R. Initial assessment of Ni-base alloy performance in 0.1 MPa and supercritical CO_2. *JOM* **67**, 2615–2620 (2015).
13. Takeyama, M. Novel concept of austenitic heat resistant steels strengthened by intermetallics. *Mater. Sci. Forum* **539-543**, 3012–3017 (2007).
14. Tan, L. et al. Corrosion of austenitic and ferritic-martensitic steels exposed to supercritical carbon dioxide. *Corros. Sci.* **53**, 3273–3280 (2011).
15. Liang, Z. et al. Corrosion performance of heat-resisting steels and alloys in supercritical carbon dioxide at 650 °C and 15 MPa. *Energy* **175**, 345–352 (2019).
16. Young, D. J. et al. Penetration of protective chromia scales by carbon. *Scr. Mater.* **77**, 29–32 (2014).
17. Gui, Y., Liang, Z. & Zhao, Q. Corrosion and carburization behavior of heat-resistant steels in a high-temperature supercritical carbon dioxide environment. *Oxid. Met* **92**, 123–136 (2019).
18. Gui, Y. et al. Corrosion behavior and lifetime prediction of VM12, Sanicro 25 and Inconel 617 in supercritical carbon dioxide at 600 °C. *Corros. Sci.* **175**, 108870 (2020).
19. Brady, M. P. et al. Effects of minor alloy additions and oxidation temperature on protective alumina scale formation in creep-resistant austenitic stainless steels. *Scr. Mater.* **57**, 1117–1120 (2007).
20. Yamamoto, Y. et al. Alumina-forming austenitic stainless steels strengthened by laves phase and MC carbide precipitates. *Metall. Mater. Trans. A* **38**, 2737–2746 (2007).
21. Yamamoto, Y. et al. Creep-resistant, Al_2O_3-forming austenitic stainless steels. *Science* **316**, 433 (2007).
22. Brady, M. P. et al. The development of alumina-forming austenitic stainless steels for high-temperature structural use. *JOM* **60**, 12 (2008).
23. Yamamoto, Y. et al. Alloying effects on creep and oxidation resistance of austenitic stainless steel alloys employing intermetallic precipitates. *Intermetallics* **16**, 453–462 (2008).
24. Yamamoto, Y. et al. Overview of strategies for high-temperature creep and oxidation resistance of alumina-forming austenitic stainless steels. *Metall. Mater. Trans. A* **42**, 922–931 (2010).
25. Wen, D. H. et al. Effects of Nb/Ti/V/Ta on phase precipitation and oxidation resistance at 1073 K in alumina-forming austenitic stainless steels. *Mater. Charact.* **144**, 86–98 (2018).
26. Guo, X. et al. Corrosion behavior of alumina-forming and oxide dispersion strengthened austenitic 316 stainless steel in supercritical water. *Corros. Sci.* **138**, 297–306 (2018).
27. Kofstad, P. Defects and transport properties of metal oxides. *Oxid. Met.* **44**, 3–27 (1995).
28. Brady, M. P. et al. Composition, microstructure, and water vapor effects on internal/external oxidation of alumina-forming austenitic stainless steels. *Oxid. Met.* **72**, 311–333 (2009).
29. Brady, M. P. et al. Increasing the upper temperature oxidation limit of alumina forming austenitic stainless steels in air with water vapor. *Oxid. Met.* **75**, 337–357 (2011).
30. Pint, B. A., Brese, R. G. & Keiser, J. R. Effect of pressure on supercritical CO_2 compatibility of structural alloys at 750 °C. *Mater. Corros.* **68**, 151–158 (2017).
31. He, L.-F. et al. Corrosion behavior of an alumina forming austenitic steel exposed to supercritical carbon dioxide. *Corros. Sci.* **82**, 67–76 (2014).
32. Tarigan, I. et al. Novel concept of creep strengthening mechanism using grain boundary Fe_2Nb laves phase in austenitic heat resistant steel. *MRS Online Proc. Libr.* **1295**, 317–322 (2011).
33. Brady, M. P. et al. Co-optimization of wrought alumina-forming austenitic stainless steel composition ranges for high-temperature creep and oxidation/corrosion resistance. *Mater. Sci. Eng. A* **590**, 101–115 (2014).
34. Chen, L. et al. Effect of oxygen on corrosion of an alumina-forming duplex steel in static liquid lead-bismuth eutectic at 550°C. *Corros. Sci.* **189**, 10959 (2021).
35. Wang, H. et al. Corrosion behaviour of Al-added high Mn austenitic steels in molten lead bismuth eutectic with saturated and low oxygen concentrations at 450 °C. *Corros. Sci.* **175**, 109591 (2020).
36. Peterson, A. & Baker, I. Microstructural evolution of Fe–20Cr–30Ni–2Nb–5Al AFA steel during creep at 760 °C. *Mater. Sci. Eng. A* **806**, 140602 (2021).
37. Suzuki, S. et al. Damage evaluation of SCC in primary loop recirculation system pipe. *Maintenology* **3**, 65–70 (2004).
38. Kim, S. H., Cha, J.-H. & Jang, C. Corrosion and creep behavior of a Ni-base alloy in supercritical-carbon dioxide environment at 650 °C. *Corros. Sci.* **174**, 108843 (2020).
39. Sridharan, K. *Corrosion of Structural Materials for Advanced Supercritical Carbon-Dioxide Brayton Cycle* 1–10 (Department of Energy, 2017).
40. Olivares, R. I. et al. Resistance of high-nickel, heat-resisting alloys to air and to supercritical CO_2 at high temperatures. *Oxid. Met.* **90**, 1–25 (2018).
41. Pint, B. A., Brese, R. G. & Keiser, J. R. Effect of pressure on supercritical CO_2 compatibility of structural alloys at 750 °C. *Mater. Corros.* **68**, 151–158 (2017).
42. Lee, H. J. et al. Corrosion and carburization behavior of chromia-forming heat resistant alloys in a high-temperature supercritical-carbon dioxide environment. *Corros. Sci.* **99**, 227–239 (2015).
43. Shi, H. et al. The influence of Y and Nb addition on the corrosion resistance of Fe-Cr-Al-Ni model alloys exposed to oxygen-containing molten Pb. *Corros. Sci.* **179**, 109152 (2021).
44. Shi, H. et al. Oxidation behavior and microstructure evolution of alumina-forming austenitic & high entropy alloys in steam environment at 1200 °C. *Corros. Sci.* **170**, 108654 (2020).
45. Shen, L. et al. Reason for negative effect of Nb addition on oxidation resistance of alumina-forming austenitic stainless steel at 1323 K. *Corros. Sci.* **191**, 109754 (2021).

46. Zhao, W. X. et al. Ultrahigh stability and strong precipitation strengthening of nanosized NbC in alumina-forming austenitic stainless steels subjecting to long-term high-temperature exposure. *Mater. Sci. Eng. A* **738**, 295–307 (2018).
47. Ha, V. T. & Jung, W. S. Creep behavior and microstructure evolution at 750° C in a new precipitation-strengthened heat-resistant austenitic stainless steel. *Mater. Sci. Eng. A* **558**, 103–111 (2012).
48. Abbasi, E. & Dehghani, K. Hot tensile properties of CoCrFeMnNi(NbC) compositionally complex alloys. *Mater. Sci. Eng. A* **772**, 138771 (2020).
49. Wei, B. Effect of NbC content on microstructure and mechanical properties of W-NbC composites. *Int. J. Refract. Met. Hard Mater.* **70**, 66–76 (2018).
50. Zhang, S. et al. Dual role of nanosized NbC precipitates in hydrogen embrittlement susceptibility of lath martensitic steel. *Corros. Sci.* **164**, 108345 (2020).
51. Xue, Y. et al. Determination of solid solubility products of [Nb][C] in the case and the core of high-temperature carburizing steel by extraction phase analysis method. *Mater. Lett.* **310**, 131519 (2022).
52. Garcia, M. P. et al. Quantitative analysis of Nb in solid solution in low carbon steels by atom probe tomography and inductively coupled plasma mass spectroscopy. *Mater. Charact.* **179**, 111308 (2021).
53. Zhang, Y. et al. Effects of annealing temperature on the microstructure, textures and tensile properties of cold-rolled Fe–13Cr–4Al alloys with different Nb contents. *Mater. Sci. Eng. A* **798**, 140236 (2020).
54. Qaban, A. et al. The effect of Al and Nb contents, cooling rate and rolling condition on the microstructure and corrosion behaviour of HSLA steel. *Mater. Today Commun.* **25**, 101362 (2020).
55. He, K., Wang, Y. & Wang, H. Influence of dynamic strain aging on ferritic/martensitic steel and stability analysis. *Fusion Eng. Des.* **171**, 112581 (2021).
56. Furukawa, T., Inagaki, Y. & Aritomi, M. Compatibility of FBR structural materials with supercritical carbon dioxide. *Prog. Nucl. Energy* **53**, 1050–1055 (2011).
57. Furukawa, T. & Rouillard, F. Oxidation and carburizing of FBR structural materials in carbon dioxide. *Prog. Nucl. Energy* **82**, 136–141 (2015).
58. Chen, H. et al. Corrosion behaviors of four stainless steels with similar chromium content in supercritical carbon dioxide environment at 650 °C. *Corros. Sci.* **156**, 16–31 (2019).
59. Liang, Z. et al. Corrosion performance of heat-resisting steels and alloys in supercritical carbon dioxide at 650 °C and 15 MPa. *Energy* **175**, 345–352 (2019).
60. Oleksak, R. P. et al. Effect of surface finish on high-temperature oxidation of steels in CO_2, supercritical CO_2, and air. *Oxid. Met* **92**, 525–540 (2019).
61. Li, H. & Chen, W. Stability of $MnCr_2O_4$ spinel and Cr_2O_3 in high temperature carbonaceous environments with varied oxygen partial pressures. *Corros. Sci.* **52**, 2481–2488 (2010).
62. Nguyen, T. D. et al. Atom probe study of impurity segregation at grain boundaries in chromia scales grown in CO_2 gas. *Corros. Sci.* **132**, 125–135 (2018).
63. Yue, X. et al. Evolution and characterization of the film formed on super 13Cr stainless steel in CO_2-saturated formation water at high temperature. *Corros. Sci.* **163**, 108277 (2020).
64. Liu, H. et al. Revealing the temperature effects on the corrosion behaviour of 2205 duplex stainless steel from passivation to activation in a CO_2-containing geothermal environment. *Corros. Sci.* **187**, 109495 (2021).
65. Cheng, S.-Y., Kuan, S.-L. & Tsai, W.-T. Effect of water vapor on annealing scale formation on 316 SS. *Corros. Sci.* **48**, 634–649 (2006).
66. Brumm, M. W., Grabke, H. J. & Wagemann, B. The oxidation of NiAl-III. Internal and intergranular oxidation. *Corros. Sci.* **36**, 37–53 (1994).
67. Shida, Y. et al. Development of preferential intergranular oxides in nickel-aluminum alloys at high temperatures. *Oxid. Met* **18**, 93–113 (1982).
68. Stott, F. H. & Wood, G. C. Internal oxidation. *Mater. Sci. Technol.* **4**, 1072–1078 (1988).
69. Li, J., et al. Effect of Cold Work on the Corrosion Resistance of an Austenitic Stainless Steel. In *Characterization of Minerals, Metals, and Materials 2016*, (eds Ikhmayies, S. J. et al.) 127–133 (Springer International Publishing, Cham, 2016).
70. Young, D. J., High Temperature Oxidation and Corrosion of Metals. In *Corrosion Series,* (ed Tim, B.) 1–10 (Elsevier, 2008).
71. Guo, X. et al. A research on the corrosion and stress corrosion cracking susceptibility of 316L stainless steel exposed to supercritical water. *Corros. Sci.* **127**, 157–167 (**2017**).
72. Tan, L., Allen, T. R. & Yang, Y. Corrosion behavior of alloy 800H (Fe–21Cr–32Ni) in supercritical water. *Corros. Sci.* **53**, 703–711 (2011).
73. Lozano-Perez, S. et al. The role of cold work and applied stress on surface oxidation of 304 stainless steel. *Corros. Sci.* **56**, 78–85 (2012).
74. Zieliński, W. & Kurzydłowski, K. TEM studies of the oxide scales formed on type 316 stainless steel during annealing at 600 C in a vacuum and air. *Scr. Mater.* **43**, 33–37 (2000).
75. Qiao, Q. et al. Effects of Nb on stress corrosion cracking of high-strength low-alloy steel in simulated seawater. *Int. J. Hydrogen Energy* **44**, 27962–27973 (2019).
76. Mazzei, G. B. et al. Effect of stress and surface finish on Pb-caustic SCC of alloy 690TT. *Corros. Sci.* **187**, 109462 (2021).
77. Du, X. S. et al. Pre-strain enhances film rupture to promote SCC of brass in Mattsson's solution—a proposal for a film-rupture-induced SCC mechanism. *Corros. Sci.* **69**, 302–310 (2013).
78. Andresen, P. L., Ford, F. P., Prediction of stress corrosion cracking (SCC) in nuclear power systems. In *Stress Corrosion Cracking*, (eds Raja, V. S., Shoji, T.,) 3–89 (Woodhead Publishing, 2011).
79. Chen, K. et al. Effect of cold work on the stress corrosion cracking behavior of Alloy 690 in supercritical water environment. *J. Nucl. Mater.* **498**, 117–128 (2018).
80. Zhong, X., Bali, S. C. & Shoji, T. Accelerated test for evaluation of intergranular stress corrosion cracking initiation characteristics of non-sensitized 316 austenitic stainless steel in simulated pressure water reactor environment. *Corros. Sci.* **115**, 106–117 (2017).
81. Lynch, S. P. Mechanistic and fractographic aspects of stress-corrosion cracking (SCC). In *Stress Corrosion Cracking*, (eds Raja, V. S., Shoji, T.,) 3–89 (Woodhead Publishing, 2011).
82. Scully, J. C. The interaction of strain-rate and repassivation rate in stress corrosion crack propagation. *Corros. Sci.* **20**, 997–1016 (1980).
83. Lynch, S. P. Progression markings, striations, and crack-arrest markings on fracture surfaces. *Mater. Sci. Eng. A—Struct*. **A468-470**, 74–80 (2007).

ACKNOWLEDGEMENTS

This work is financially supported by Shanghai Pujiang Program with granted number 2020PJD022. National Research and Development Program of China (No. 2018YFE0116200), Nature Science Foundation of China (No. 12105175); Postdoctoral Sustentation Fund, China (No. 2021TQ0199). Thanks to the microstructural characterization of Instrumental Analysis Center of SJTU.

AUTHOR CONTRIBUTIONS

X.G. and Z.M. conceived and designed the experiments; Z.L. performed the SSRT tests; S.C. performed the analytical experiments and wrote the manuscript under the supervision of X.G. and L.Z., Z.M. assisted the tests. All authors contributed to the scientific discussion of the results and reviewed the manuscript.

COMPETING INTERESTS

The authors declare no competing interests.

ADDITIONAL INFORMATION

Correspondence and requests for materials should be addressed to Xianglong Guo.

Reprints and permission information is available at http://www.nature.com/reprints

Publisher's note Springer Nature remains neutral with regard to jurisdictional claims in published maps and institutional affiliations.